ACS APPLIED MATERIALS & INTERFACES

Research Article

www.acsami.org

# Direct Observation of Dopants Distribution and Diffusion in GaAs Planar Nanowires with Atom Probe Tomography

Jiangtao Qu,[†] Wonsik Choi,[§] Parsian Katal Mohseni,[§] Xiuling Li,[§] Yingjie Zhang,[∥] Hansheng Chen,[†] Simon Ringer,[‡] and Rongkun Zheng*[,†]

[†]School of Physics and [‡]School of Aerospace, Mechanical and Mechatronic Engineering, The University of Sydney, Sydney, New South Wales 2006, Australia

[§]Department of Electrical and Computer Engineering, Micro and Nanotechnology lab, University of Illinois, Urbana, Illinois 61801, United States

[∥]Australian Nuclear Science and Technology Organisation, Locked Bag 2001, Kirrawee DC, New South Wales 2232, Australia

Supporting Information

**ABSTRACT:** Intentional and unintentional doping in semiconductor nanowires undoubtedly have significant impact on the device performance. However, spatially resolved precise determination of dopant concentration is challenging due to insufficient sensitivity and resolution of conventional techniques. In this paper, quantitative 3D distribution of Si and Zn dopants in planar GaAs nanowires and their interface with AlGaAs film underneath are obtained by using a unique atom probe tomography technique, providing critical insights for the growth and potential applications of these nanowires.

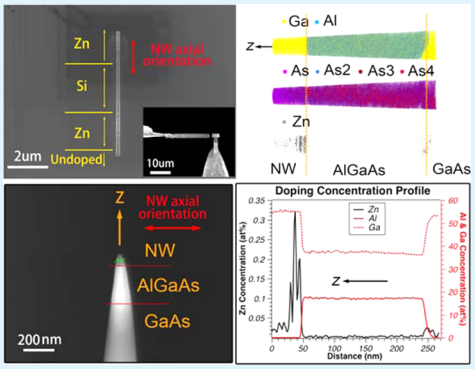


**KEYWORDS:** *planar GaAs nanowires, NWs, APT, FIB, tomography, doping*

## 1. INTRODUCTION

Semiconductor nanowires (NWs), catalytically grown out of plane in accordance with the substrate orientation on the basis of vapor−liquid−solid (VLS) mechanism,[1] have demonstrated unique properties for various applications and therefore have attracted considerable attention in recent years.[2−10] So far, experimental research efforts have demonstrated the potential of semiconductor NWs for numerous device applications, such as 135% performance improvement on metal oxide semiconductor field effect transistors (MOSFETs) made from semiconductor NWs by taking advantage of their defect-free state and high aspect ratios,[11] lower threshold for laser emission from GaN NWs,[12] and enhanced power conversion efficiency of various NW-based solar cells due to their inherent light-trapping capability,[13,14] and so on. However, two problems hinder the commercial development of devices with vertical NWs to boost the performance of integrated circuits (ICs). The first obstacle lies in how to make these out-of-plane vertical NWs compatible with current planar lithographic processing technology. The second obstacle is that apart from additional processing complexity involved in laying down vertical NWs without damage the deficiency in NWs' transferring and precisely positioning capabilities make it impossible to manufacture very large scale ICs.[15,16] The recent emergence of planar NWs seems to rekindle the prospect of commercial applications with these pseudo-1D materials.[17−20] One efficient approach to grow these planar NWs is based on selective lateral epitaxy (SLE): With the help of metallic Au catalyst, GaAs NWs can be grown via SLE in-plane along <110> directions on (100) substrate, and their position can be precisely controlled by accurately placing the catalyst with prepatterning,[21−23] which is able to address the two problems mentioned above. Moreover, the feasibility of this materials on various devices was proved by recent successful fabrication of high electron mobility transistors.[21,22,24]

However, intentional doping and unintentional impurities arising from NW synthesis and IC manufacture processing have significant impacts on the performance of devices. The intentional doping enables functionalization of semiconductor NWs for various purposes. However, unintentional impurities can degrade the performance of devices,[25,26] such as forming deep level recombination centers and leading to negative effects on electronics, photonics, and optoelectronics.[27−30] These adverse doping effects are usually unintentional and occur at low concentrations which cannot be detected by traditional characterizing technique due to their insufficient sensitivity and resolution. Capable of volumetrically mapping elements of materials in both quantitative and qualitative aspects with better

Received: July 20, 2016
Accepted: September 16, 2016
Published: September 16, 2016




DOI: 10.1021/acsami.6b08919
ACS Appl. Mater. Interfaces 2016, 8, 26244−26250

than 0.3 nm spatial resolution in all direction, atom probe tomography (APT) provides atomic-level insights into materials.[31−33] In this paper, GaAs planar NWs intentionally doped with silicon and zinc were grown on a thin $Al_{0.3}GaAs$ film on top of a GaAs (100) substrates by MOCVD, and APT experiments were carried out to quantitatively determine the doping distribution in the epilayers and interfaces.

## 2. MATERIALS AND METHODS

In our experiment, GaAs (100) substrates were used for the growth of GaAs planar NWs by SLE. However, in order to distinguish the GaAs NWs on the GaAs (100) substrates considering homogeneous elemental composition, $Al_{0.3}GaAs$ buffer layer (~200 nm) was initially grown on GaAs (100) by introducing $1.17 \times 10^{-4}$ mol/min trimethylgallium (TMGa), $3.57 \times 10^{-5}$ mol/min trimethylaluminum (TMAl), and $3.71 \times 10^{-3}$ mol/min arsine ($AsH_3$) for 84 s prior to the onset of NW growth by MOCVD in an Aixtron 200/4 horizontal flow MOCVD reactor. Thereafter, planar GaAs NWs were grown in the reactor under atmospheric pressure. TMGa and $AsH_3$ were used as precursors for Ga and As, respectively, $H_2$ was used as the carrier gas, and 250 nm Au colloids were used as SLE seeding agents. Before the TMGa precursor was introduced, samples were heated up and kept at 625 °C for 10 min under $AsH_3$ flow. Thereafter, both TMGa and $AsH_3$ were introduced for GaAs NWs growth at 460 °C. During growth, $1.79 \times 10^{-6}$ and $3.57 \times 10^{-6}$ mol/min of disilane ($Si_2H_6$) and $8.56 \times 10^{-7}$ and $9.78 \times 10^{-7}$ and $1.10 \times 10^{-6}$ mol/min of diethylzinc (DEZn) as doping precursors were introduced for 30 s in alternating sequence for n-type and p-type segment formation on GaAs NWs as shown in Figure 1a. From Figure 1b, the periodically twinned regions of the NWs were identified as the p-type segments doped with Zn, while nontwinned regions were identified as n-type doped with Si. The reason for notched morphology observed in the p-type segments is due to twin plane defects correlated with Zn doping,[24] which can also be found in vertical NWs.[34] However, there is an incubation period at Zn-doped NW segment before the periodic corrugations are exhibited, which cannot be observed in the nontwinned region.[35] In addition, the Au catalysts on the head of NWs was removed by sonication.

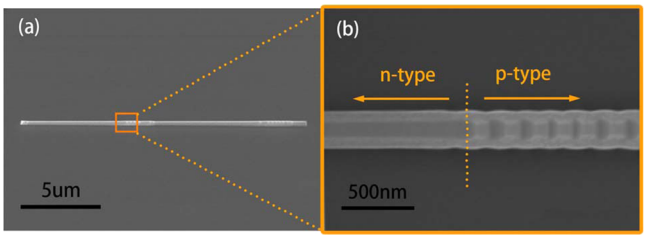


**Figure 1.** (a) Tilted view (20°) of single entire planar GaAs NWs on AlGaAs. (b) Zoom-in image of the yellow rectangle in panel a shows p-type segment doped with Zn and n-type with Si (0° tilted view).

The APT specimen preparation was carried out with Zeiss Auriga SEM/FIB by a lift-out process. As illustrated in Figure 2, regions of interest (ROI) were first marked with Pt dots beside the NWs. Electron and ion beam depositions were then carried out in turns for approximately 1 $\mu$m thick Pt as the protective layer to avoid ion beam damage during the subsequent FIB process. After that, the wedge with single NW was lifted out and transferred to a pretreated Mo tip by Pt bonding. Finally, annular milling was allowed to carefully proceed for the final formation of tip around 50 nm thickness with ROI accurately placed on the vertices. Considering the multilayer structure of the GaAs(NW)/AlGaAs/GaAs(substrate) sample which is prone to rupture under the electrical force in APT, 15 nm of nickel was coated by sputtering in an ion beam sputtering/etching (IBs/e) system for strengthening.

## 3. RESULTS AND DISCUSSION

The position and orientation of the needle-shaped APT specimen with regard to the layered sample is shown in Figure 3a. The GaAs NWs doped with Zn or Si sandwiched between AlGaAs and Pt layers. Pt was deposited with sequential electron and ion beams showing different contrast, which ensures deposition efficiency and quality. The corresponding diffraction pattern (zone axis <011>) shown in Figure 3b was acquired by JEOL TEM 2200, confirming perfect zinc blend single crystallization of the sample.

APT experiments were carried out with a CAMECA local electrode atom probe (LEAP) 4000X SI at 23 K with laser energy of 12 pJ and pulse frequency of 200 kHz. Afterward, field evaporation commenced around 3200 kV. Because the multilayer specimen is vulnerable to electric force, the specimen doped with Si was coated with nickel to secure the interfacial bonding.

The geometry and structure of APT specimen is shown in Figure 4a. The specimen in the inset was prepared perpendicular to the NW axial orientation and AlGaAs surface with a NW/AlGaAs/GaAs substrate configuration. The tomo-

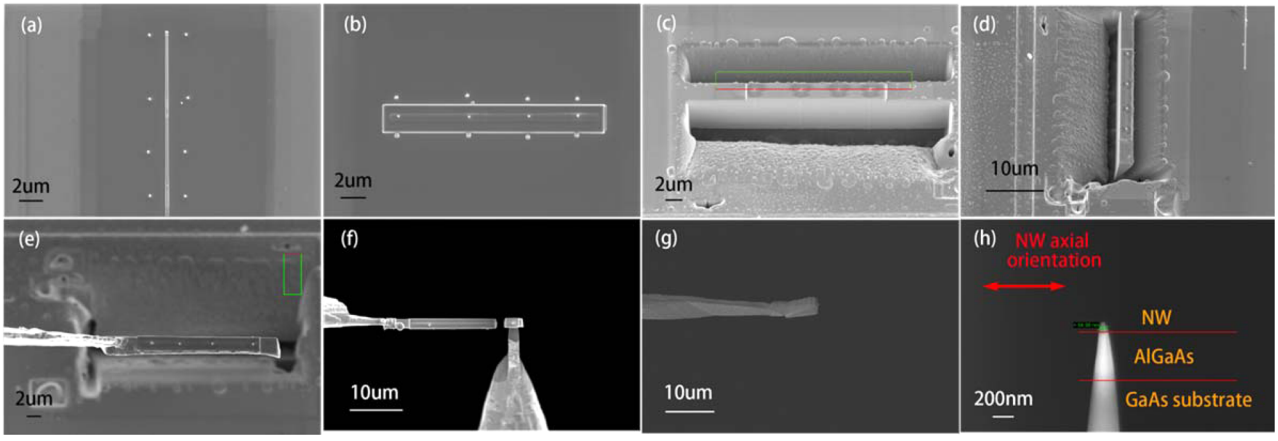


**Figure 2.** Specimen preparation procedure. (a) Tilted view (0°) of selected ROI, and (b) Pt deposition for protection. (c) Tilted SEM view (24°) of wedge cutting. (d) Detaching wedge from substrate (10° tilted view). (e) Wedge lifting out (10° tilted view). (f) Wedge transferring (10° tilted view). (g) Specimen bonding with Mo tip by Pt deposition (20° tilted view). (h) Annular milling for ~50 nm thickness tip formation (54° tilted view).



DOI: 10.1021/acsami.6b08919
ACS Appl. Mater. Interfaces 2016, 8, 26244−26250

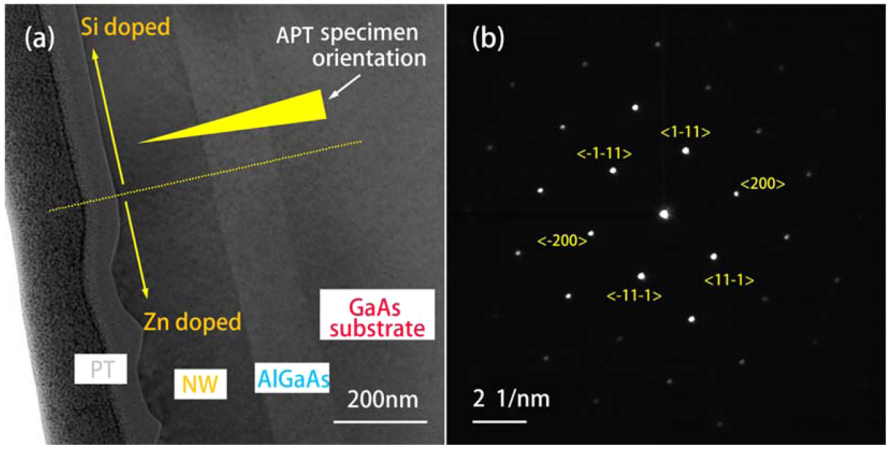


**Figure 3.** (a) TEM image showing schematic position and orientation of the APT specimen relative to the planar NW. (b) Diffraction pattern of the sample (zone axis <011>).

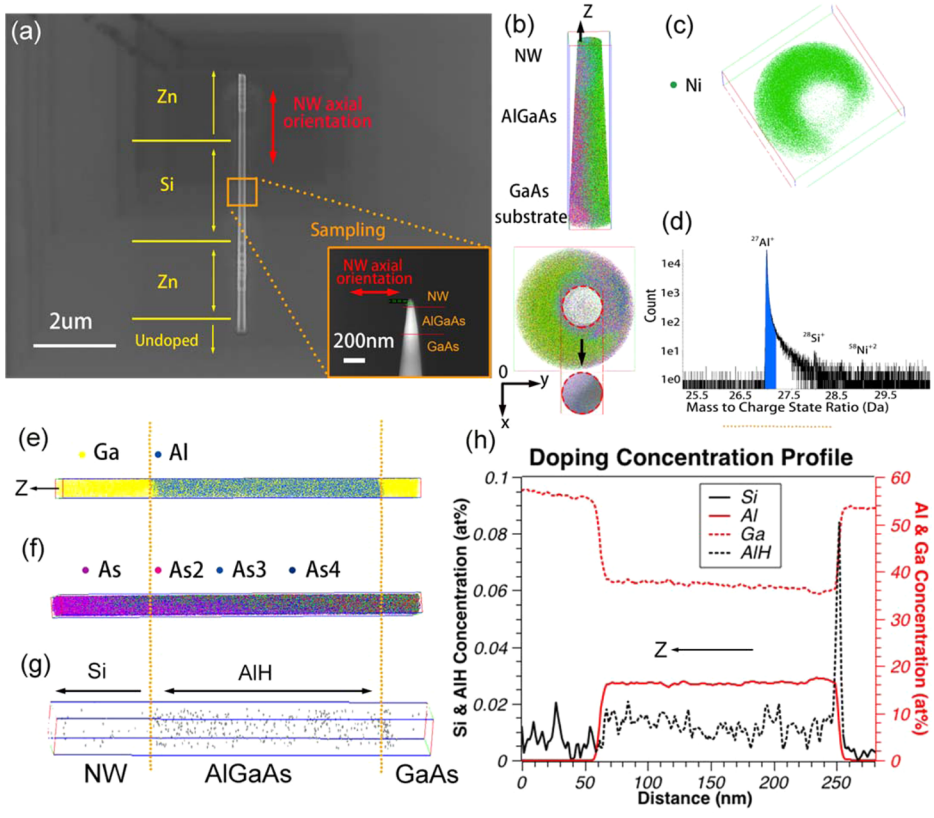


**Figure 4.** Reconstruction of Si-doped specimen. (a) Tilted SEM image (0°) showing location of the specimen. (The inset showing the geometry and structure of APT specimen). (b) Reconstruction of the specimen and new column-shaped ROI. (c) Protective nickel shell (top view of panel b via z direction). (d) Mass spectrum of selected region around Si peak for new ROI in panel b. (e) Ga and Al, (f) As and its clusters, and (g) Si distribution in the new ROI defined in panel b. (h) 1D concentration profile of Si, Al, Ga, and AlH cluster along APT specimen. (3D tomography movies of Si-doped specimen: Movies S1, S2, and S3).

graphic image of Si-doped specimen shown in Figure 4b clearly revealed the Ni shell and entire GaAs NW core. Normally, only the core of the specimen can be collected due to local aperture in APT; however, the presence of Ni shell in Figure 4c enables the full collection of GaAs NW. In order to unveil the Ni shell and target NW for analysis only, a new column-shaped ROI was defined as shown in the bottom of Figure 4b. Consequently, a 200 nm thick Al-enriched layer (blue region) can be found within the AlGaAs region in Figure 4e, which is equivalent with TEM observation. Meanwhile, As was prone to evaporation as clusters due the polar and anisotropic nature of GaAs as shown in Figure 4f. Apart from other elements, a tiny peak of mass spectrum can be found at the positon of $^{28}Si$ in Figure 4d, which proves the existence of the Si in this new ROI. The length of the NW region is about 60 nm, and its interface with AlGaAs was indicated by the sharp increase in Al concentration at 60 nm in Figure 4h. However, the detected NW region is smaller than the thickness of the NW observed in TEM in Figure 3a, representing that the outer surface of the NW had been milled away. Therefore, the Si concentration profile in


DOI: 10.1021/acsami.6b08919
ACS Appl. Mater. Interfaces 2016, 8, 26244−26250

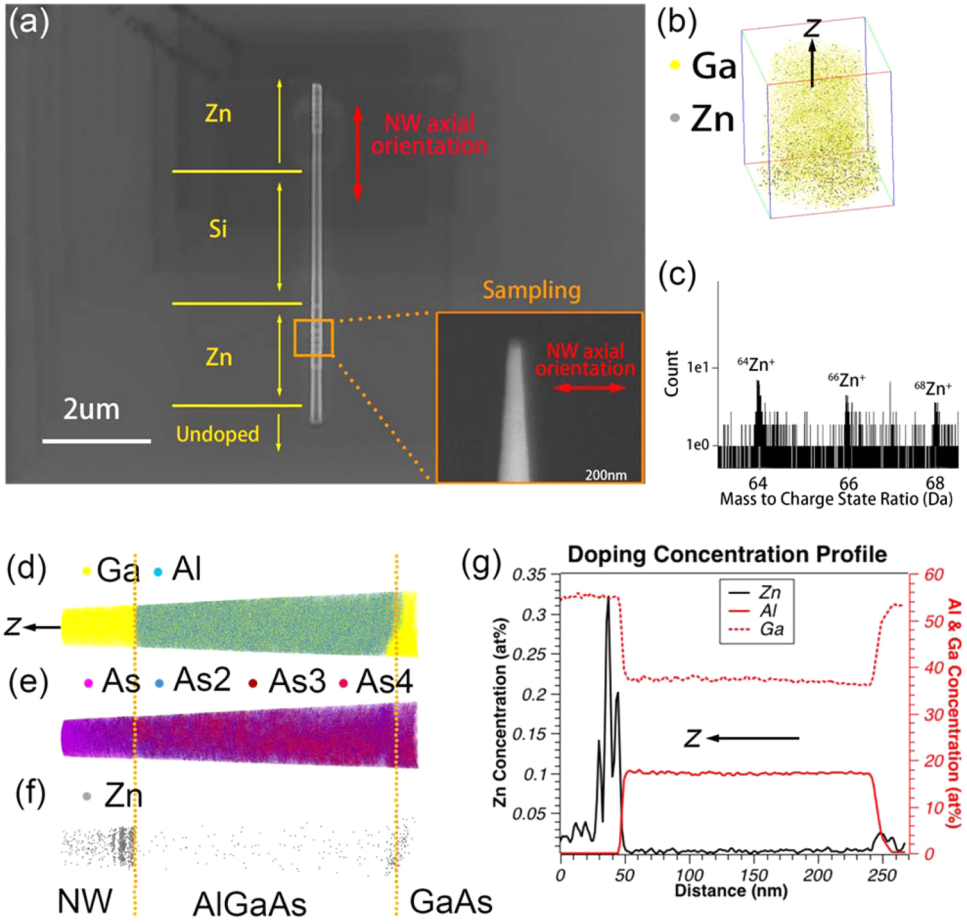


**Figure 5.** Reconstruction of Zn-doped GaAs. (a) Tilted SEM image (0°) showing location of the specimen. (The inset shows the needle-shaped APT specimen.) (b) Ga and Zn in NW segment. (c) Mass spectrum of selected region around Zn peak. (d) Al and Ga and (e) As and its clusters distribution along NWs, AlGaAs, and partly GaAs substrate. (f) Zn distribution along specimen, AlGaAs, and substrate. (g) 1D concentration profile of Zn, Al, and Ga. (3D tomography movies of Zn-doped specimens: Movies S4, S5, and S6)

Figure 4h ranges from a certain place under NW surface to the NW/AlGaAs interface. Si and Ga have a ratio of $4.15 \times 10^{-5}$ in the NW segment. Interestingly, Figure 4g shows higher Si atom density in AlGaAs compared with that in the NW segment, which seems to be contradictory with the real scenario, given that AlGaAs film was not intentionally doped with any element. This can be explained with the mechanism of APT, which is based on time-of-flight mass spectrometry. As cluster composed of a single $^{27}Al$ atom and a single $^{1}H$ with one charge has the same mass charge ratio as a single $^{28}Si^{+}$ atom; therefore, APT regarded them as same element.[36] Another aspect is that the concentration of Al in AlGaAs is 2000 times larger than that of Si in NW segment; therefore, $^{27}Al^{1}H^{+}$ has higher concentration compared to that of Si, which are represented by black dashed and black solid lines, respectively, in Figure 4h. In addition, a noticeable $^{27}Al^{1}H^{+}$ peak at 250 nm demonstrates the presence of considerable H arisen from $HCl/H_2O$ (1:1) etching before AlGaAs formation on GaAs substrate. Considering the high probability of extrinsic Ga incorporation into NW during specimen preparation with FIB, it is reasonable to see a declined trend of Ga concentration which is indicated by red dashed line in Figure 4h.

The results of the Zn-doped segment are shown in Figure 5. The AlGaAs layer in Figure 5d is 200 nm in length, which is consistent with the measurement in TEM. Unsurprisingly, the As evaporated as larger clusters with increasing voltage, which was shown in Figure 5e. As the tip of specimen was consumed and became shorter, the apex became blunt; therefore, higher voltage was needed to keep constant field evaporation. Meanwhile, two Zn-enriched layers were discovered close to the boundary between the NW and AlGaAs layer and interface of AlGaAs and GaAs, as revealed in Figure 5f,g. This implies that Zn preferentially resides at the interface due to trapping by local interfacial defects and dislocations as shown in Figure S1. However, the small peak at the AlGaAs/GaAs interface around 250 nm is attributed to the diffusion of Zn during NW growth.[37,38] The ratio between Zn and Ga in the NW segment is $1.59 \times 10^{-3}$ as shown in Figure 5b. According to the eutectic diagram system of Au−Zn and Au−Si,[39,40] Zn has higher solubility than does Si in Au at 460 °C; therefore, the concentration of Si should be lower than that of Zn in NWs, which is in agreement with our experiment. Another point is that we did not find any Si-enriched layer at the interface as Zn did; this can be attributed to low Si doping in NWs due to limited solubility of Si in gold. Furthermore, Si is less diffusive than Zn; therefore, it is difficult to identify the Si-enriched layer with the influence of $^{27}Al^{1}H^{+}$ at interfaces.

However, our planar NW in Figures 1a and 4a shows a slight tapering shape along the growth direction, which indicates the concurrence of a VS parasitic thin film growth and axial VLS NW growth. In our experiment, the temperature for NW growth was set up at 460 °C which is higher than the pyrolysis


DOI: 10.1021/acsami.6b08919
ACS Appl. Mater. Interfaces 2016, 8, 26244−26250

temperature of TMGa, DEZn, and $AsH_3$;[41−43] therefore, Zn can directly grow on the surface of substrate in the form of thin film by VS mechanism without Au catalyst involved. It is reasonable to expect that there is also a Zn-enriched layer at the NW/AlGaAs interface under the Si-doped NW segment marked by yellow rectangle in Figure 4a. However, the specimen with Si doping was sputtered with Ni before APT experiment, and the positions of Ni isotopes and $^{64}Zn^+$ overlap in the mass spectrum. A new ROI was defined carefully to exclude the Ni impact at maximal extent, which is shown in Figure 4b. The results in Figure 6 confirm the existence of Zn-

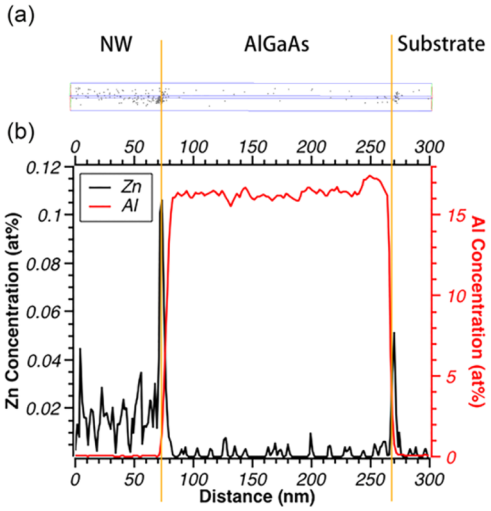


**Figure 6.** Zn and Al concentration in Si-doped NW segment. (a) Zn distribution and (b) Zn and Al 1D concentration along NW, AlGaAs layer, and substrate.

enriched layer at NW/AlGaAs interface in Si-doped NW segment, and this is because that the entire AlGaAs surface was exposed to the Zn precursor before Si-doped NW grew atop it. However, it is necessary to point out that the black line in Figure 6b cannot accurately represent the concentration of Zn in specimen due to the fact that the impact of Ni cannot be completely eliminated by the new ROI as indicated by the tiny spike in the Figure 4d. Therefore, the black trend line in Figure 6b represents the sum of Ni and Zn concentration. In addition, the new column shape ROI was defined to fit the NW region on tapering shape specimen; consequently, the periphery of AlGaAs and GaAs substrates were excluded outside the ROI. It is reasonable to believe that NW region has more Ni impact.

Also, there is no remarkable Zn concentration observed in AlGaAs region. During the growth of Zn-doped NW region, lots of Zn incorporated into NW via VLS and accumulated at its interface with AlGaAs by diffusion. However, a few Zn atoms could go through this interface and enter AlGaAs layers. Considering that AlGaAs film is only ~200 nm thick, Zn could easily diffuse to the interface with GaAs substrate and was therefore trapped by it. Consequently, the Zn concentration baseline in AlGaAs region is lower than that in NW region.

Similarly, we also find a few Si atoms in Zn-doped NW as indicated by Figure 7. Because the growth of Zn-doped NW region is prior to that of Si-doped NW region, during Si-doped NW segment growth, Si can also grow on the surface of Zn-doped NW region as thin film due to the presence of VS mechanism. However, Si is less diffusive than Zn, so the

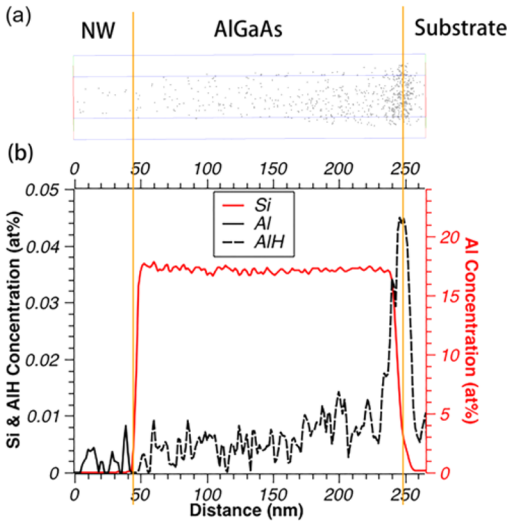


**Figure 7.** Si and Al concentration in Zn-doped NW segment. (a) Si distribution and (b) Si, Al, and $^{27}Al^1H^+$ 1D concentrations along NW, AlGaAs layer, and substrate.

concentration of Si inside NW of Zn-doped region is quite low as shown in Figure 7b.

However, as to the doping distribution in NWs, the Zn and Si exhibit a huge difference which is shown in Figure 8. The binomial and experimental distribution of Si has the same trend with a *p*-value of 0.9889, which indicates random Si distribution, whereas the *p*-value for Zn is below 0.0001, which demonstrates a nonrandom distribution of Zn.

Due to its high carrier mobility and defect-free state, planar GaAs NWs doped with Zn show potential for next-generation VLSI in nanoscale. However, considering the thin diameter of GaAs NWs, below 200 nm, the Zn-enriched layer located in the boundary between NW/AlGaAs layer has significant impacts on the performance if devices such as MOSFET are made of it. Moreover, if the diameter of planar NWs continues shrinking down to or below 100 nm according to the trend of ICs development, then the Zn-enriched layer, which is less than 100 nm from the surface, can also work as carrier pathway in conjunction with source/drain. Consequently, it will result in the degeneration of the carrier mobility by severe ionized impurity scattering. A series of problematic issues related to device electrical properties and physical isolation will arise such as gate controlling, threshold voltage, interfacial capacitance control, and isolation of active channel from substrate, among others. Therefore, a more uniform Zn distribution incorporated via catalytic pathway is desired for greater NW functionality.

## 4. CONCLUSIONS

APT provides deep insights into materials including identifying lightly doped regions at the nanometer scale, which cannot be discerned by traditional techniques. In this paper, we have demonstrated a FIB-based specimen preparation method for planar NWs and quantitatively determined the spatial distribution of impurity dopants in different segments of the NW specimen by APT. The ratio between Si and Ga is $4.15 \times 10^{-5}$ ($\sim 1 \times 10^{17}$ $cm^{-3}$) in the n-type segment of NWs, whereas that of Zn and Ga is $1.59 \times 10^{-3}$ ($\sim 5 \times 10^{18}$ $cm^{-3}$) in the p-type segment. In addition, two Zn-enriched layers at NW/AlGaAs interface and AlGaAs/GaAs interface were observed. Note that the GaAs planar nanowire sample contains 8 p−n


DOI: 10.1021/acsami.6b08919
ACS Appl. Mater. Interfaces 2016, 8, 26244−26250

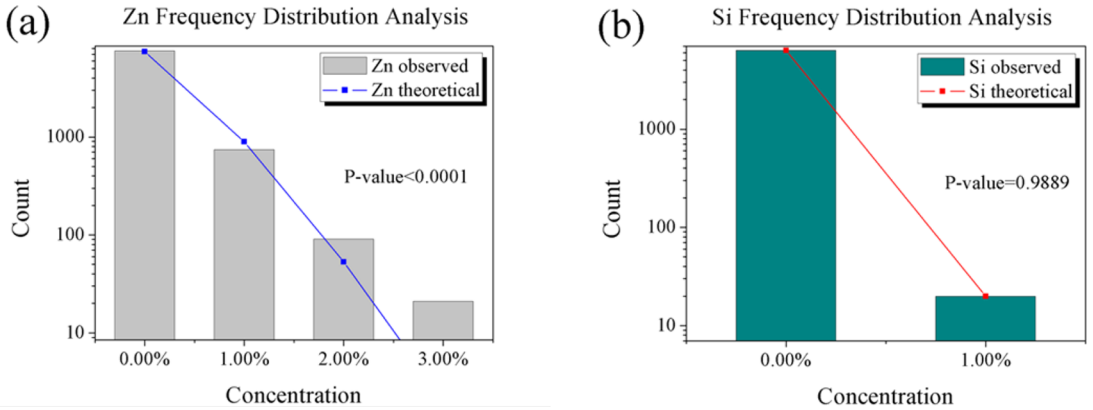


**Figure 8.** Comparison of experimental and binomial doping distribution in NW segment. (a) Zn frequency distribution. (b) Si frequency distribution.

junctions and the first grown junction, i.e., the segment that experienced the longest thermal treatment, was the one that was probed by APT.

Given that Zn is an extremely diffusive dopant, its relationship with growth temperature can be expressed as $D = D_0\, e^{-E_A/(kT)}$, where $D_0$ is the maximum diffusion coefficient, $E_A$ is the activation energy, $T$ is the absolute temperature, and $k$ is the Boltzmann constant. Obviously, the diffusion coefficient is proportional to temperature. In order to yield planar GaAs nanowires with the devices' preferable Zn doping distribution, the NW growth temperature and growth duration can be slightly tuned downward to suppress the Zn diffusion and its incorporation into NWs via the VS mechanism.

## ■ ASSOCIATED CONTENT

### Supporting Information

The Supporting Information is available free of charge on the ACS Publications website at DOI: 10.1021/acsami.6b08919.

TEM images of interfacial defects and dislocations in NWs and at its interface with AlGaAs (PDF)

Movie S1: 3D tomography movie of Ga atoms and Al atoms in Si-doped specimen (MOV)

Movie S2: 3D tomography movie of As atoms in Si-doped specimen (MOV)

Movie S3: 3D tomography movie of Si atoms in Si-doped specimen (MOV)

Movie S4: 3D tomography movie of Ga atoms and Al atoms in Zn-doped specimen (MOV)

Movie S5: 3D tomography movie of As atoms in Zn-doped specimen (MOV)

Movie S6: 3D tomography movie of Zn atoms in Zn-doped specimen (MOV)

## ■ AUTHOR INFORMATION


### Corresponding Author

*E-mail: rongkun.zheng@sydney.edu.au.

### Present Address

P.K.M.: Microsystems Engineering, Rochester Institute of Technology, Rochester, NY 14623, United States.



### Funding

This research was supported by Australian Research Council (DP150100018) and the U.S. National Science Foundation DMR Grant No. 15-08140.


### Notes

The authors declare no competing financial interest.

## ■ ACKNOWLEDGMENTS


We acknowledge the facilities and technical assistances from the Australian Institute of Nuclear Science and Engineering, Australian Nuclear Science and Technology Organisation, and the Australian Microscopy & Microanalysis Research Facility at the University of Sydney. X.L. acknowledges the support from the U.S. National Science Foundation DMR Grant No. 15-08140.


## ■ REFERENCES


(1) Wagner, R. S.; Ellis, W. C. Vapor-Liquid-Solid Mechanism of Single Crystal Growth. *Appl. Phys. Lett.* **1964**, *4* (5), 89−90.

(2) Jung, C. S.; Kim, H. S.; Jung, G. B.; Gong, K. J.; Cho, Y. J.; Jang, S. Y.; Kim, C. H.; Lee, C.-W.; Park, J. Composition and Phase Tuned InGaAs Alloy Nanowires. *J. Phys. Chem. C* **2011**, *115* (16), 7843−7850.

(3) Jenichen, A.; Engler, C. Reconstructions and Surface Facets of the GaAs(112)A and (112)B Surfaces: First-Principles DFT Supercell Calculations. *Surf. Sci.* **2013**, *608*, 204−211.

(4) Bellew, A. T.; Manning, H. G.; Gomes da Rocha, C.; Ferreira, M. S.; Boland, J. J. Resistance of Single Ag Nanowire Junctions and Their Role in the Conductivity of Nanowire Networks. *ACS Nano* **2015**, *9* (11), 11422−11429.

(5) Dorodnyy, A.; Alarcon-Lladó, E.; Shklover, V.; Hafner, C.; Fontcuberta i Morral, A.; Leuthold, J. Efficient Multiterminal Spectrum Splitting via a Nanowire Array Solar Cell. *ACS Photonics* **2015**, *2* (9), 1284−1288.

(6) Fu, A.; Gao, H.; Petrov, P.; Yang, P. Widely Tunable Distributed Bragg Reflectors Integrated into Nanowire Waveguides. *Nano Lett.* **2015**, *15* (10), 6909−6913.

(7) Im, J.-H.; Luo, J.; Franckevičius, M.; Pellet, N.; Gao, P.; Moehl, T.; Zakeeruddin, S. M.; Nazeeruddin, M. K.; Grätzel, M.; Park, N.-G. Nanowire Perovskite Solar Cell. *Nano Lett.* **2015**, *15* (3), 2120−2126.

(8) Chen, L.; Cai, F.; Otuonye, U.; Lu, W. D. Vertical Ge/Si Core/Shell Nanowire Junctionless Transistor. *Nano Lett.* **2016**, *16* (1), 420−426.

(9) Sadaf, S. M.; Ra, Y. H.; Szkopek, T.; Mi, Z. Monolithically Integrated Metal/Semiconductor Tunnel Junction Nanowire Light-Emitting Diodes. *Nano Lett.* **2016**, *16* (2), 1076−1080.

(10) Wu, J.; Babadi, A. S.; Jacobsson, D.; Colvin, J.; Yngman, S.; Timm, R.; Lind, E.; Wernersson, L.-E. Low Trap Density in InAs/High-k Nanowire Gate Stacks with Optimized Growth and Doping Conditions. *Nano Lett.* **2016**, *16* (4), 2418−2425.

(11) Luong, G. V.; Knoll, L.; Blaeser, S.; Süess, M. J.; Sigg, H.; Schäfer, A.; Trellenkamp, S.; Bourdelle, K. K.; Buca, D.; Zhao, Q. T.;

Mantl, S. Demonstration of Higher Electron Mobility in Si Nanowire MOSFETs by Increasing the Strain Beyond 1.3%. *Solid-State Electron.* **2015**, *108*, 19−23.
(12) Gradečak, S.; Qian, F.; Li, Y.; Park, H.-G.; Lieber, C. M. GaN Nanowire Lasers with Low Lasing Thresholds. *Appl. Phys. Lett.* **2005**, *87* (17), 173111−173113.
(13) Mohseni, P. K.; Behnam, A.; Wood, J. D.; Zhao, X.; Yu, K. J.; Wang, N. C.; Rockett, A.; Rogers, J. A.; Lyding, J. W.; Pop, E.; Li, X. Monolithic III-V Nanowire Solar Cells on Graphene via Direct Van Der Waals Epitaxy. *Adv. Mater.* **2014**, *26* (22), 3755−3760.
(14) Mallorquí, A. D.; Alarcón-Lladó, E.; Russo-Averchi, E.; Tütüncüoglu, G.; Matteini, F.; Rüffer, D.; Morral, A. F. i. Characterization and Analysis of InAs/p−Si Heterojunction Nanowire-Based Solar Cell. *J. Phys. D: Appl. Phys.* **2014**, *47* (39), 394017−394025.
(15) Dowdy, R.; Walko, D. A.; Fortuna, S. A.; Li, X. Realization of Unidirectional Planar GaAs Nanowires on GaAs (110) Substrates. *IEEE Electron Device Lett.* **2012**, *33* (4), 522−524.
(16) Dowdy, R. S.; Walko, D. A.; Li, X. Relationship Between Planar GaAs Nanowire Growth Direction and Substrate Orientation. *Nanotechnology* **2013**, *24* (3), 035304−035310.
(17) Shen, Y.; Turner, S.; Yang, P.; Van Tendeloo, G.; Lebedev, O. I.; Wu, T. Epitaxy-Enabled Vapor−Liquid−Solid Growth of Tin-Doped Indium Oxide Nanowires with Controlled Orientations. *Nano Lett.* **2014**, *14* (8), 4342−4351.
(18) Nikoobakht, B. Toward Industrial-Scale Fabrication of Nanowire-Based Devices. *Chem. Mater.* **2007**, *19* (22), 5279−5284.
(19) Zi, Y.; Jung, K.; Zakharov, D.; Yang, C. Understanding Self-Aligned Planar Growth of InAs Nanowires. *Nano Lett.* **2013**, *13* (6), 2786−2791.
(20) Zhang, C.; Miao, X.; Mohseni, P. K.; Choi, W.; Li, X. Site-Controlled VLS Growth of Planar Nanowires: Yield and Mechanism. *Nano Lett.* **2014**, *14* (12), 6836−6841.
(21) Miao, X.; Chabak, K.; Zhang, C.; Katal Mohseni, P.; Walker, D., Jr.; Li, X. High-Speed Planar GaAs Nanowire Arrays with $f > 75$ GHz by Wafer-Scale Bottom-up Growth. *Nano Lett.* **2015**, *15* (5), 2780−2786.
(22) Zhang, C.; Li, X. Planar GaAs Nanowire Tri-Gate MOSFETs by Vapor−Liquid−Solid Growth. *Solid-State Electron.* **2014**, *93*, 40−42.
(23) Fortuna, S. A.; Wen, J.; Chun, I. S.; Li, X. Planar GaAs Nanowires on GaAs (100) Substrates: Self-Aligned, Nearly Twin-Defect Free, and Transfer-Printable. *Nano Lett.* **2008**, *8* (12), 4421−4427.
(24) Miao, X.; Zhang, C.; Li, X. Monolithic Barrier-All-Around High Electron Mobility Transistor with Planar GaAs Nanowire Channel. *Nano Lett.* **2013**, *13* (6), 2548−2552.
(25) Putnam, M. C.; Filler, M. A.; Kayes, B. M.; Kelzenberg, M. D.; Guan, Y.; Lewis, N. S.; Eiler, J. M.; Atwater, H. A. Secondary Ion Mass Spectrometry of Vapor−Liquid−Solid Grown, Au-Catalyzed, Si Wires. *Nano Lett.* **2008**, *8* (10), 3109−3113.
(26) Bullis, W. M. Properties of Gold in Silicon. *Solid-State Electron.* **1966**, *9* (2), 143−168.
(27) Wang, X.; Yang, X.; Du, W.; Ji, H.; Luo, S.; Yang, T. Thickness Influence of Thermal Oxide Layers on The Formation of Self-Catalyzed InAs Nanowires on Si(111) by MOCVD. *J. Cryst. Growth* **2014**, *395*, 55−60.
(28) Riley, J. R.; Bernal, R. A.; Li, Q.; Espinosa, H. D.; Wang, G. T.; Lauhon, L. J. Atom Probe Tomography of a-Axis GaN Nanowires: Analysis of Nonstoichiometric Evaporation Behavior. *ACS Nano* **2012**, *6* (5), 3898−3906.
(29) Kasapoglu, E.; Duque, C. A.; Şakiroğlu, S.; Sari, H.; Sökmen, İ. The Effects of the Intense Laser Field on Donor Impurities in a Cylindrical Quantum Dot under the Electric Field. *Phys. E* **2011**, *43* (8), 1427−1432.
(30) Allen, J. E.; Hemesath, E. R.; Perea, D. E.; Lensch-Falk, J. L.; Li, Z. Y.; Yin, F.; Gass, M. H.; Wang, P.; Bleloch, A. L.; Palmer, R. E.; Lauhon, L. J. High-Resolution Detection of Au Catalyst Atoms in Si Nanowires. *Nat. Nanotechnol.* **2008**, *3* (3), 168−173.
(31) Kelly, T. F.; Larson, D. J. Atom Probe Tomography 2012. *Annu. Rev. Mater. Res.* **2012**, *42* (1), 1−31.
(32) Cerezo, A.; Clifton, P. H.; Galtrey, M. J.; Humphreys, C. J.; Kelly, T. F.; Larson, D. J.; Lozano-Perez, S.; Marquis, E. A.; Oliver, R. A.; Sha, G.; Thompson, K.; Zandbergen, M.; Alvis, R. L. Atom Probe Tomography Today. *Mater. Today* **2007**, *10* (12), 36−42.
(33) Qu, J.; Ringer, S.; Zheng, R. Atomic-Scale Tomography of Semiconductor Nanowires. *Mater. Sci. Semicond. Process.* **2015**, *40*, 896−909.
(34) Algra, R. E.; Verheijen, M. A.; Borgstrom, M. T.; Feiner, L.-F.; Immink, G.; van Enckevort, W. J. P.; Vlieg, E.; Bakkers, E. P. A. M. Twinning Superlattices in Indium Phosphide Nanowires. *Nature* **2008**, *456* (7220), 369−372.
(35) Dowdy, R. S.; Zhang, C.; Mohseni, P. K.; Fortuna, S. A.; Wen, J.-G.; Coleman, J. J.; Li, X. Perturbation of Au-assisted planar GaAs nanowire growth by p-type dopant impurities. *Opt. Mater. Express* **2013**, *3* (10), 1687−1697.
(36) Gault, B.; Moody, M. P.; Cairney, J. M.; Ringer, S. P. *Atom Probe Microscopy*, 2012 ed; Springer-Verlag: New York, New York, 2012.
(37) Reichert, W.; Chen, C. Y.; Li, W. M.; Shield, J. E.; Cohen, R. M.; Simons, D. S.; Chi, P. H. Incorporation of Zn in GaAs during Organometallic Vapor Phase Epitaxy Growth Compared to Equilibrium. *J. Appl. Phys.* **1995**, *77* (5), 1902−1906.
(38) Ky, N. H.; Pavesi, L.; Araújo, D.; Ganière, J. D.; Reinhart, F. K. A Model for the Zn Diffusion in GaAs by a Photoluminescence Study. *J. Appl. Phys.* **1991**, *69* (11), 7585−7593.
(39) Okamoto, H.; Massalski, T. B. The Au-Si(Gold-Silicon) System. *Bull. Alloy Phase Diagrams* **1983**, *4* (2), 190−198.
(40) Okamoto, H.; Massalski, T. B. The Au-Zn (Gold-Zinc) System. *Bull. Alloy Phase Diagrams* **1989**, *10* (1), 59−69.
(41) Li, S. H.; Larsen, C. A.; Chen, C. H.; Stringfellow, G. B.; Brown, D. W. Dimethylarsine: Pyrolysis Mechanisms and Use for OMVPE Growth. *J. Electron. Mater.* **1990**, *19* (4), 299−304.
(42) Francis, J. T.; Benson, S. W.; Tsotsis, T. T. Kinetics of the Very Low Pressure Pyrolysis of Trimethylgallium and Arsine. *J. Cryst. Growth* **1991**, *112* (2), 474−486.
(43) Thiandoume, C.; Sallet, V.; Triboulet, R.; Gorochov, O. Decomposition Kinetics of Tertiarybutanol and Diethylzinc Used as Precursor Sources for the Growth of ZnO. *J. Cryst. Growth* **2009**, *311* (5), 1411−1415.


DOI: 10.1021/acsami.6b08919
*ACS Appl. Mater. Interfaces* 2016, 8, 26244−26250